THESIS FOR THE DEGREE OF LICENTIATE OF PHILOSOPHY

Raman spectroscopy on neat and doped conjugated polymers

Local dynamics and relaxation processes

Giannis G. Gkikas

Department of Chemistry and Chemical Engineering
CHALMERS UNIVERSITY OF TECHNOLOGY
Göteborg, Sweden 2026

Raman spectroscopy on neat and doped conjugated polymers

Local dynamics and relaxation processes

Giannis G. Gkikas

Licentiatuppsatser vid Institutionen för kemi och kemiteknik

Chalmers tekniska högskola

Nr 2026:11

Department of Chemistry and Chemical Engineering
Chalmers University of Technology
SE-412 96 Göteborg
Telephone +46 31 772 1000

Cover:
Raman microscopy image of the g_3TT monomer under 532 nm laser excitation.

Printed by Chalmers digitaltryck
Göteborg, Sweden 2026

Raman spectroscopy on neat and doped conjugated polymers
Local dynamics and relaxation processes
Giannis G. Gkikas
Department of Chemistry and Chemical Engineering
Chalmers University of Technology

Abstract

Conjugated polymers are a class of materials that combine the mechanical flexibility and processability of conventional polymers with tunable electronic properties. The backbone of conjugated polymers consists of alternating single and double bonds, creating a delocalized π-electron system that enables charge transport. While these materials are intrinsically semiconducting, their electrical conductivity can be significantly enhanced through chemical or electrochemical doping, making them suitable for a wide range of semiconducting applications. In addition to their electronic functionality, conjugated polymers retain the advantageous mechanical properties of soft materials, such as flexibility and low weight. Importantly, both the mechanical and electronic properties are highly dependent on the chemical structure, including the backbone design and the nature of the side chains, which influence molecular packing, intermolecular interactions, and overall material morphology.

In this work, Raman spectroscopy is employed as the primary analytical technique to investigate the structural, electronic, and vibrational properties of a thienothiophene-based conjugated polymer functionalized with polar triethylene glycol side chains. Raman spectroscopy is particularly well suited for studying conjugated systems due to its sensitivity to molecular vibrations associated with the π-conjugated backbone, enabling detailed insights into bonding, conjugation length, and doping-induced structural changes. An experimental methodology for the assignment of vibrational modes is presented, combining spectral analysis with systematic variations in experimental conditions to accurately identify characteristic vibrational signatures.

Temperature-dependent Raman measurements are further employed to probe the thermal behavior of the polymer, providing insight into dynamic processes such as molecular relaxation and the glass transition. In addition, the potential of spatially resolved Raman mapping is explored as a powerful tool for investigating heterogeneities within the material, particularly in relation to localized doping phenomena.

Keywords: conjugated polymers, doping, Raman spectroscopy, relaxation processes, glass transition

List of Publications

This thesis is based on the following appended papers, referred to by Roman numerals in the text:

I. Linking the evolution of Raman active vibrational modes to the glass transition of a polymer mixed conductor

Giannis G. Gkikas , Elsa Veronica Flores-Vela, Mariavittoria Craighero, Joost Kimpel, Christian Müller, and Anna Martinelli

Chemistry of Materials, **(2026)**, *submitted*

II. Gold-activated persulfate p-doping of organic semiconductors

Tiefeng Liu, Matilde Silveri, Zesheng Liu, Sang Young Jeong, Qiao He, Giannis G. Gkikas , Wenlong Jin, Chi-Yuan Yang, Tom P. A. van der Pol, Feng Zhang, Christina Kousseff, Anna Martinelli, Iain McCulloch, Martin Heeney, Han Young Woo, Alessandro Motta, Mats Fahlman, and Simone Fabiano

Nature Materials, 25 **(2026)**, 02547

My contribution to the publications

Paper I

I was responsible for the experimental assignment of vibrational modes based on Raman spectroscopy, as well as performing temperature dependent Raman measurements. I carried out all data analysis by fitting procedures. In addition, I wrote the first draft of the manuscript and contributed to the preparation of the final version together with my co-authors.

Paper II

I was responsible for the design and execution of Raman mapping experiments. I performed the data analysis and interpretation of the results, and contributed to the review of the manuscript.

Additional publications which are not included in the thesis:

Static and Dynamic Disorder in Formamidinium Lead Bromide Single Crystals

Guy Reuveni, Yael Diskin-Posner, Christian Gehrmann, Shravan Godse, Giannis G. Gkikas , Isaac Buchine, Sigalit Aharon, Roman Korobko, Constantinos C. Stoumpos, David A. Egger, and Omer Yaffe

The Journal of Physical Chemistry Letters, 13 **(2022)**, 10767–10773

Vacancy-Ordered Quadruple Halide Perovskites: All-Inorganic Nobel-Metals Semiconductors with Infrared Absorption

Alaelddin Michailidis Barakat, Rafaela Maria Giappa, Giannis G. Gkikas , Emmanouil G. Manidakis, George Volonakis, Myung-Gil Kim, and Constantinos C. Stoumpos

Chemistry of Materials, 38 **(2026)**, 4466–4480

Acknowledgements

First of all, I would like to thank the Knut and Alice Wallenberg Foundation for their financial support.

I would like to express my gratitude to my supervisor, Anna Martinelli, for her guidance and valuable scientific discussions throughout this work. I also thank Christian Müller, project leader, for his insightful discussions and for his collaborative research group.

I am grateful to my co-supervisor Eva Olsson, my examiner Per-Anders Carlsson, and the director of studies Ergang Wang for their support and contributions.

I would also like to thank all my colleagues on the 2nd and 3rd floor for creating such a pleasant working environment. In addition, I appreciate the colleagues on the 8th floor, who are always willing to engage in discussions about conjugated polymers.

Special thanks go to those with whom I shared the closest connections: my officemate Nicole, as well as Jesper and Luigi, for their constant support and companionship.

Finally, I would like to thank Emma for always being by my side, and my family for their support.

Giannis G. Gkikas, Göteborg, May 2026

Contents

List of Figures

List of Tables

1 Introduction

The modern plastic bag, invented in the early 1960s in Norrköping (Sweden), by Sten Gustaf Thulin at the packaging company Celloplast AB [1], represents one of the most successful applications of a conventional synthetic polymer such as polyethylene (PE) [2]. Polyethylene and related polyolefins are valued for their low density, mechanical durability, chemical resistance, and excellent electrical insulating properties, which arise from their saturated hydrocarbon backbones [3].

Conventional polymers consist of σ-bonded carbon–carbon and carbon–hydrogen chains, lacking the extended π-conjugation required for efficient electric charge transport [4]. As a result, while they are mechanically robust and inexpensive, their electronic functionality is inherently limited.

A fundamental breakthrough occurred with the discovery that certain polymers containing conjugated backbones could support electronic charge transport (which was awarded the Nobel Prize 2000 Figure 1.1) [5]. Rather than emerging from an existing demand for flexible electronics, the invention and understanding of conjugated polymers opened entirely new possibilities for combining mechanical flexibility with electronic properties.

Figure 1.1: The Nobel Prize laureates in Chemistry 2000 awarded for the discovery and development of conductive polymers.

This marked the emergence of conductive polymers, which retain the mechanical advantages of traditional plastics while introducing electrical conductivity, hence making them essential for applications such as flexible electronics, energy devices, and bioelectronic interfaces [6].

The properties of conjugated polymers are inherently governed by thermodynamic principles, as their chemical structure responds to external stimuli such as temperature and mechanical deformation [7].

This thesis explores the interplay between chemical structure and thermodynamics, emphasizing their critical role in governing material behavior and, ultimately, determining the properties and performance of the final functional product.

1.1 Why do we need conductive polymers?

Conductive polymers are important because they combine the advantageous properties of both polymers and metals, offering a unique class of materials that traditional systems cannot easily replicate. Unlike conventional inorganic conductors such as metals or semiconductors, conductive polymers provide a lightweight, flexible, and potentially low-cost alternative, making them highly attractive for modern technologies (Figure 1.2) [8]. By being organic–inorganic materials, they bridge the gap between rigid electronic components and soft, processable plastics [9].

Figure 1.2: Conductive polymers have a wide range of applications, including photovoltaics, transistors, display emitters, sensing and biosensing technologies, light-emitting diodes (LEDs), and thermoelectric generators (TEGs).

One of their key strengths is their tunability, i.e. their electrical, optical, and mechanical properties can be tailored through chemical design, enabling a wide range of different applications. This versatility is particularly valuable in the development of flexible and stretchable organic optoelectronic devices, such as wearable electronics, foldable displays, and lightweight solar cells, where traditional materials fall short.

1.1.1 Applications

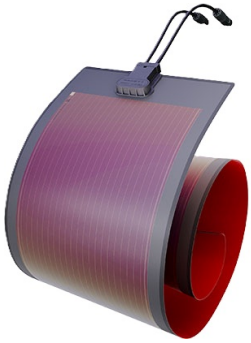

Figure 1.3: Example of a flexible organic solar panel produced by Heliatek. Adapted from Ref. [10].

Conductive polymers have found widespread applications across several advanced technologies due to their unique combination of electrical conductivity, flexibility, and tunable properties. In solar cells, particularly organic photovoltaics, they serve as active layers that enable lightweight and flexible energy harvesting devices (Figure 1.3). In organic field-effect transistors (OFETs), conductive polymers function as semiconducting channels, allowing for low-cost and large-area electronic circuits. Their sensitivity to environmental changes makes them highly suitable for sensing and biosensing applications, where they can detect chemical or biological signals with high responsiveness [11]. Additionally, in batteries and other energy devices, conductive polymers are used to improve charge transport and enhance performance, contributing to the development of more efficient and adaptable energy solutions [12].

Background 2

2.1 Conjugated polymers

Conjugated polymers, also known as conductive polymers, are a class of polymeric materials characterized by an alternating sequence of single and double bonds along their carbon backbone. This conjugated structure results in a system of delocalized π-electrons, where the overlapping p-orbitals create an electron-rich pathway along the chain [13, 14]. As a result, charge carriers can move more freely compared to the case of conventional insulating polymers, giving rise to electrical conductivity [15]. This unique electronic structure is what distinguishes conjugated polymers from conventional polymers and enables their use in electronic and optoelectronic applications.

2.1.1 Different types of conjugated polymers

Conjugated polymers can be broadly classified according to their dominant charge transport behavior and their chemical backbone structure. From an electronic perspective, they are commonly divided into p-type and n-type materials [16]. Conjugated **n-type** polymers support electron transport and incorporate electron-deficient structural units that stabilize negative charge carriers.[1] In contrast, **p-type** conjugated polymers predominantly conduct holes and are typically based on electron-rich backbones with high-lying HOMO (highest occupied molecular orbital) energy levels.[2] Based on their chemical structure, conjugated polymers can be classified into several distinct families, among which thiophene-based polymers (Figure 2.1) are particularly prominent due to their high charge carrier mobility. This class of polymers constitutes the primary focus of this thesis. In particular, Paper I centers on the polymer poly(3,6-bis(2-methoxyethoxy)-2-methyl-5-(5′-methyl-[2,2′-bithiophen]-5-yl)thieno[3,2-*b*]thiophene), abbreviated as p(g_3TT–T2) (Figure 2.1 a).

1: Examples of **n-type** polymers are naphthalene diimide (NDI) and perylene diimide (PDI) moieties.

2: Examples of **p-type** polymers are polythiophenes, poly(3-hexylthiophene) (P3HT), polyaniline, and poly(p-phenylene vinylene) (PPV).

2.2 Doped conjugated polymers

Intrinsic conjugated polymers typically behave as electrical insulators or low-conductivity semiconductors. In other words, although their conjugated structure provides a pathway for charge transport, their conductivity remains limited in the undoped state. However, due to their unique chemical structure, these polymers can

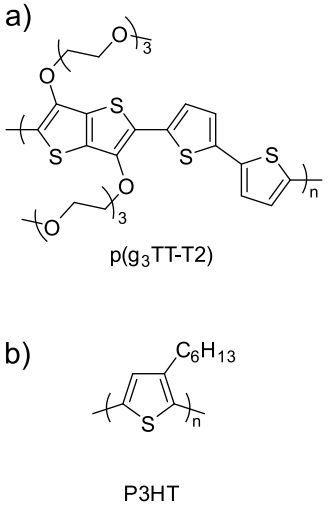

Figure 2.1: Molecular structure of a) p(g_3TT-T2) and b) P3HT.

undergo chemical or electrochemical oxidation or reduction processes, known as doping [17]. During doping, charge carriers such as positive polarons (p-doping) or negative polarons (n-doping) are introduced into the polymer backbone, significantly increasing electronic conductivity.[3] This process transforms the material from a poorly conducting polymer to a highly conductive one, making it suitable for various electronic applications.

3: The electronic conductivity of conjugated polymers in their undoped state typically lies in the range of 10^{-9} to 10^{-5} S cm^{-1}. Upon high levels of doping, their conductivity can reach values between 10^{-5} and 10^{3} S cm^{-1} [18–20].

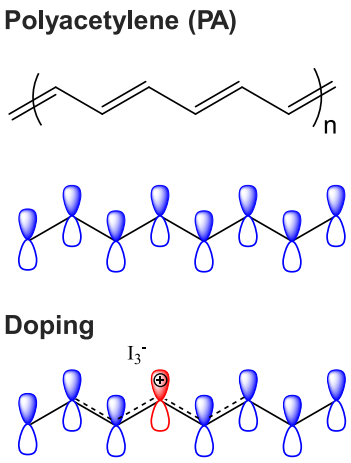

Figure 2.2: Molecular structure of polyacetylene (PA) together with a schematic representation of the delocalized π-electron system along its conjugated backbone. Chemical doping with iodine vapors is illustrated as a representative example, where triiodide ions (I_3^-) are formed and act as counterions to compensate the positive charges generated on the polymer chain, thereby maintaining charge neutrality.

2.2.1 Doping methods

In conjugated polymers, doping is the key method used to generate mobile charge carriers and transform these materials from electrical insulators into conducting materials. Because conjugated polymers have delocalized π-electron backbones, their electrical conductivity can be drastically increased by introducing dopants that either remove or add electrons. The two principal approaches are chemical doping and electrochemical doping, which differ fundamentally in how charge carriers are introduced and control doping levels (Figure 2.2).

Chemical doping involves the incorporation of electron-accepting or electron-donating species directly into the polymer, typically through exposure to dopant molecules, vapors, or solutions. In p-type chemical doping, oxidizing agents remove electrons from the polymer backbone, generating positive charge carriers (polarons or bipolarons),[4] while the dopant becomes a counterion that stabilizes the charge. Common p-type dopants include halogens (such as iodine), strong Lewis acids, or molecular oxidants like $FeCl_3$ and $F4TCNQ$ (Figure 2.3 a). Chemical doping is typically simple to apply, scalable, and suitable for bulk processing, but it offers limited control over the exact doping level and can lead to structural disorder, phase separation, or dopant diffusion over time, which affects long term stability.

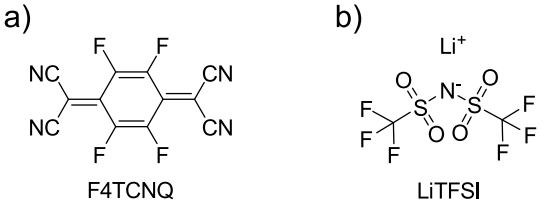

Figure 2.3: Chemical structure of a) F4TCNQ and b) LiTFSI.

4: A polaron is a quasiparticle formed when a charge (electron or hole) interacts with, and locally distorts, the molecular structure. A bipolaron, in contrast, consists of two charges bound together within a shared lattice distortion, giving rise to a coupled state characterized by a larger structural deformation and a total charge of $\pm 2e$ [21].

5: LiTFSI is a common electrolyte salt that dissociates into Li^+ and $TFSI^-$ ions in non-aqueous solutions. In Ref. [22], H-TFSI was used for sequential doping, whereas in Ref. [23], it was employed for electrochemical doping.

In contrast, electrochemical doping introduces charge carriers by applying an external electrical potential to the conjugated polymer while it is in contact with an electrolyte[5] (Figure 2.3 b). When a positive potential is applied, the polymer is oxidized (p-doped). To maintain charge neutrality, ions from the electrolyte migrate into the polymer matrix as counterions. Electrochemical doping is inherently reversible and controllable, allowing the doping level to be tuned precisely by the applied voltage. This method is widely used in fundamental studies of charge transport, redox

behavior, and ion-electron coupling, as well as in applications such as electrochromic devices, organic batteries, and organic electrochemical transistors [24].

The key distinction between the two methods lies in control and reversibility. Chemical doping is generally irreversible and fixed once the dopant is introduced, making it suitable for devices that require permanent conductivity. Electrochemical doping, on the other hand, is dynamic and reversible, enabling real-time modulation of conductivity and optical properties.

In summary, the choice of dopant in chemical doping of conjugated polymers requires careful consideration of energy alignment, safety and application constraints, as well as long-term stability. Optimizing these factors is essential for electronic properties of conjugated polymers to be developed into robust and practical electronic devices.

2.3 Thermal properties of conjugated polymers

The thermal properties of conjugated polymers critically affect their processability, performance, and long term stability in organic electronic devices. Thermal stability governs the retention of chemical structure and electronic functionality at elevated temperatures, while degradation such as backbone or side chain degradation, oxidation, or dopant loss typically occurs above 200 °C and reduces electrical and mechanical performance [25]. Controlled thermal annealing below the degradation threshold can enhance molecular ordering, π–π stacking, and charge transport, whereas excessive heating may cause phase separation or dopant redistribution. Achieving a balance between thermal robustness and processability through polymer design and doping control is therefore essential for reliable device operation.

From a thermodynamic perspective, a first–order phase transition exhibits continuous first derivatives of the Gibbs free energy but discontinuities in second derivatives, such as the heat capacity, and does not involve latent heat. While conjugated polymers may exhibit transitions or transformations that resemble classical thermodynamic phase behavior, many relevant thermal phenomena including the glass transition and annealing induced structural reorganization are governed by non-equilibrium and kinetic effects. In this thesis, I aim to highlight the importance of understanding these thermal processes and transition phenomena in conjugated polymers, and how they can be investigated using vibrational spectroscopy.

2.3.1 Thermal expansion

Thermal expansion is the tendency of a material to change its dimensions when its temperature changes. As temperature increases, atoms or molecular segments vibrate more strongly and explore larger average separations due to anharmonic bonding, leading to an increase in length, area or volume.

2.3.2 Melting and Annealing

In conjugated polymers, the melting temperature (T_m) marks a limit beyond which morphological changes occur, compromising thermal stability and accelerating degradation in devices [26].

The annealing temperature plays a crucial role in determining the polymer microstructure. Studies have shown that appropriate thermal annealing enhances molecular ordering and crystallinity [26], leading to increased charge-carrier mobility [27].

2.3.3 Glass transition

The glass transition temperature (T_g) is the temperature at which an amorphous material changes from a rigid, glassy state to a soft, rubbery state due to increased molecular mobility [28]. It is a key parameter governing mechanical behavior, processability, and safe operating conditions.

Although often described as a second–order transition,[6] the glass transition is not a true thermodynamic phase transition. It is a non–equilibrium, kinetic process in which the system falls out of equilibrium as molecular relaxation times exceed the experimental timescale. As a result, the glassy state is a kinetically frozen, non–equilibrium state rather than a distinct thermodynamic phase.

6: The glass transition is sometimes referred to as a pseudo second–order transition [29]. A second-order transition is an equilibrium phase change with smooth entropy change but a sudden change in properties like heat capacity. Meanwhile, the pseudo second-order looks similar but actually comes from cooling-rate-dependent kinetic freezing rather than a true phase change.

2.3.4 Dynamic fragility

Dynamic fragility (m) quantifies how sharply the molecular dynamics of a glass forming material slow down as the temperature approaches the glass transition temperature T_g. It distinguishes strong glass formers, which show nearly Arrhenius behavior, from fragile glass formers, which exhibit strongly non–Arrhenius behavior (Figure 2.4).

Dynamic fragility measures the sensitivity of the structural relaxation time τ (or equivalently, the viscosity η) to temperature near T_g. In strong glass formers, molecular mobility decreases gradually upon cooling, whereas in fragile glass formers the dynamics slow down dramatically as T_g is approached.

This behavior is commonly visualized using an Angell plot, in which $\log(\tau)$ (or $\log(\eta)$) is plotted as a function of the inverse reduced temperature T_g/T. The corresponding fragility index m characterizes the slope of this curve at $T = T_g$[7] [30]:

- Large m values correspond to fragile glass formers
- Small m values correspond to strong glass formers[8]

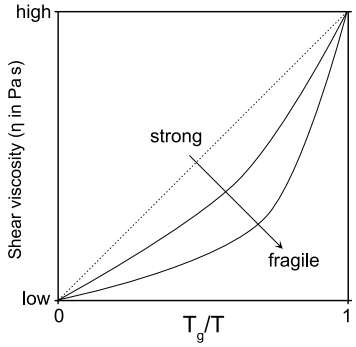

Figure 2.4: Angell plot illustrating strong and fragile glass-forming behavior via viscosity.

7: Fragility can be calculated from the slope of the curve close to T_g (see Paper I) or using the polymer's constants C_1 and C_2 (see Appendix A, Connection between fragility (Angell) and WLF).

8: For SiO_2, which is a strong glass former, m ≈ 20; while for a fragile glass former like polyethylene terephthalate (PET), m ≈ 140 [31, 32].

2.3.5 Time scale of glass transition

The glass transition occurs when the structural relaxation time reaches experimental time scales, typically $\tau \sim 10^2$–10^3 s.

Fragility describes how rapidly a material reaches this condition as the temperature decreases. As a consequence, two materials may exhibit the same glass transition temperature T_g while possessing very different fragilities, reflecting distinct underlying molecular dynamics.

2.3.6 Relaxation processes

In glass-forming materials, relaxation processes describe distinct molecular motions occurring on different time and length scales [33]. The primary α-relaxation corresponds to cooperative structural rearrangements and controls viscous flow; its characteristic time increases sharply upon cooling and reaches macroscopic timescales at the glass transition, where it becomes effectively frozen. Secondary β-relaxations persist below T_g and arise from localized molecular or segmental motions, often following an Arrhenius behavior. Finally, γ-relaxations occur at even lower temperatures and involve highly localized motions (such as short chains, polar groups or rotational motions). These relaxation processes demonstrate that molecular mobility in glasses spans a broad hierarchy of timescales, even below the glass transition.

Table 2.1: Thermal processes in conjugated polymers. I: first–order; II*: pseudo second–order; "–": not a thermodynamic phase transition.

Process	**Order**	**Equilibrium**	**Key**
Expansion	–	Yes	Constant
Annealing	–	No	Kinetic
Melting	I	Yes	Latent heat
Glass transition	II*	No	C_p
Fragility	–	No	Dynamic
Relaxation	–	No	Time

Methodology 3

3.1 Thermal investigation

Following the discussion of thermal properties in the previous chapter, this chapter focuses on the glass transition of conjugated polymers and its experimental detection.

3.1.1 Methods to investigate thermal properties

The most widely used experimental technique for detecting the glass transition is differential scanning calorimetry (DSC), where the transition appears as a step change in the heat capacity. An extension of this method, fast differential scanning calorimetry (FDSC), enables measurements at very high heating and cooling rates and is particularly useful for studying kinetic effects and materials with weak calorimetric signatures or limited sample volumes. Other approaches include ellipsometry, which determines T_g from changes in thermal expansion and film thickness and is especially well suited for thin polymer films. Dynamic mechanical thermal analysis (DMTA) provides complementary information by probing changes in viscoelastic properties and identifying the glass transition through alterations in storage and loss moduli. Measurements based on viscosity can also be used to define the glass transition, although they typically require large amounts of material and are therefore less practical for polymer thin films. Another powerful technique is broadband dielectric spectroscopy (BDS), which detects the glass transition through the temperature dependence of molecular relaxation processes. In addition, several studies have reported observations of the glass transition using spectroscopic techniques, such as Raman spectroscopy. However, in conjugated polymers, these often lack a detailed analysis of the underlying molecular dynamics. Filling this gap, a comprehensive spectroscopic investigation of the glass transition is presented in Paper I of this thesis.

3.2 Raman spectroscopy

Raman spectroscopy is a vibrational spectroscopic technique that probes molecular vibrations through the inelastic scattering of light. When monochromatic light (usually from a laser) interacts with a material, most photons are elastically scattered (Rayleigh scattering), but a small fraction exchange energy with molecular vibrational modes, leading to a shift in photon energy (Figure 3.1).

This energy shift constitutes the Raman effect. Because vibrational energies are characteristic of specific chemical bonds and molecular structures, the Raman spectrum provides a fingerprint of characteristic bonds, conformations and interactions [34].

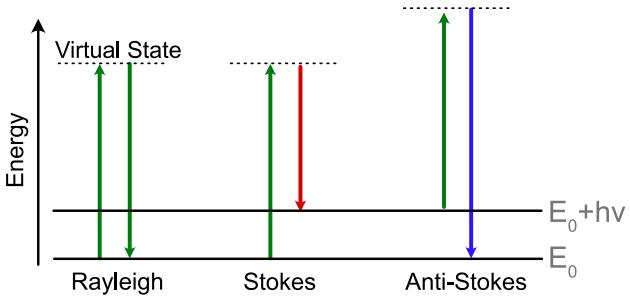

Figure 3.1: A typical Jablonski diagram representing elastic scattering (Rayleigh) and inelastic scattering with energy loss (Stokes) and energy gain (Anti-Stokes).

Table 3.1: Types of molecular vibrational modes [35].

Mode	Category	Symbol	Description
Symmetric	Stretching	ν	Two atoms move in and out synchronously
Asymmetric	Stretching	ν_{as}	Two atoms move in opposite directions in and out
Scissoring	Bending	γ or δ	Two atoms attached to a central atom move toward and away from each other like the blades of scissors
Rocking	Bending	ρ	The entire group of atoms swings back and forth in the same plane
Wagging	Bending	ω or ρ_w	The atoms bend back and forth like a windshield wiper
Twisting	Bending	τ	The atoms rotate around the bond connecting them to the rest of the molecule

A vibrational mode is Raman active if it induces a change in the molecular polarizability during the vibration of a covalent bond:

$$\left(\frac{\partial \alpha}{\partial Q}\right) \neq 0$$

where α is the molecular polarizability of the bond and Q is the normal vibrational coordinate.

As a result, Raman spectroscopy is particularly sensitive to:

- Symmetric vibrational modes
- Conjugated polymer backbones
- Delocalized π electronic systems

3.2.1 Instrumentation

Raman measurements were performed using a Renishaw *inVia*™ confocal Raman microscope operating in a back-scattering configuration (Figgure 3.2). Excitation was provided by an Ar-ion laser (532 nm, maximum output power 100 mW), a HeNe laser (633 nm, maximum output power 17 mW), or a near-infrared diode laser (785 nm, maximum output power 300 mW). The incident laser power at the sample was adjusted for each measurement in order to minimize local heating.

The microscope was equipped with Leica objective lenses of 5× (NA = 0.12), 20× (NA = 0.40), 50× (NA = 0.50), and 100× (NA = 0.75), allowing flexibility in spatial resolution and collection efficiency. Measurements were performed in confocal mode, providing enhanced lateral and axial resolution as well as enabling depth-resolved analysis.[1]

1: For a more detailed correlation between the governing equations and the corresponding experimental parameters, see Appendix A.2, *Optical parameters in Raman microscopy*.

Spectral dispersion was achieved using interchangeable diffraction gratings with 1200, 1800, and 2400 grooves/mm, selected according to the desired balance between spectral resolution and spectral range. Raman-scattered light was detected by a cooled CCD detector, ensuring low noise levels and high signal-to-noise ratios.

Temperature-dependent Raman measurements were performed using a Linkam heating/cooling stage, enabling precise control of the sample temperature during acquisition (Paper I).

Raman mapping experiments[2] were performed using a motorized XY translation stage, enabling automated spatially resolved measurements, where a full Raman spectrum was acquired at each spot on the x–y plane (Paper II).

2: The spatial resolution is limited by the diffraction-limited size of the laser spot, typically on the order of $\sim 1\mu$m, and depends on the wavelength of the excitation source and the numerical aperture of the objective.

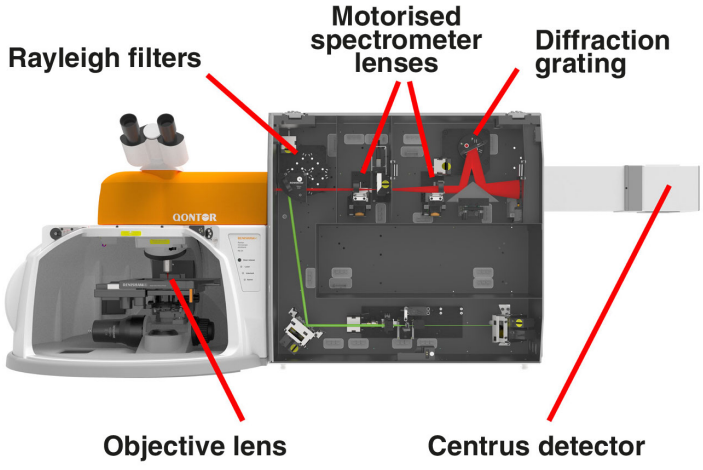

Figure 3.2: A typical optical layout for an *inVia*™ confocal Raman spectrometer. Adapted from Renishaw plc [36].

3.2.2 Laser effects

The choice of the laser wavelength is a trade-off between signal strength, fluorescence, spatial resolution, penetration depth, and

sample damage. In fact, while the Raman peak positions remain unchanged, different lasers can alter the intensity and background of the spectrum. Specifically, shorter wavelengths (e.g. 532 nm) provide stronger Raman scattering (scaling as $1/\lambda^4$) and smaller focal volumes (higher spatial resolution and smaller laser spot), but also risk to induce fluorescence and shallower penetration, whereas longer wavelengths (e.g. 785–1064 nm) can help reduce fluorescence, increase penetration depth and sampling volume, and minimize heating or damage at the cost of weaker signals. Additionally, laser choice can affect resonance Raman enhancement when the excitation matches an electronic transition, selectively amplifying certain vibrational modes. In practice, the laser is selected by balancing fluorescence suppression, required penetration depth, focal volume (linked to laser diameter), and the possibility of resonance effects for the specific material under study.

3.2.3 Sample preparation (solid, film, substrate)

The specific measurement conditions depend on whether the material is studied as a bulk solid, a thin film, or a liquid solution. Bulk polymers and powders can typically be measured directly, with the laser focused on a flat surface or representative region, although structural heterogeneity may influence spectral intensity. For thin conjugated-polymer films, precise focusing within the film is critical to enhance backbone vibrational modes while minimizing contributions from the substrate (such as silicon). In dilute or solution-processed polymers, the laser is focused within the liquid volume to avoid container artifacts, enabling to probe local chain conformation. In all cases, careful focus control and moderate laser power are essential to prevent local heating and to reliably probe the conjugated backbone structure.

3.2.4 Data treatment and analysis

The measured spectrum provides several key parameters: the Raman shift, intensity, peak area, and full width at half maximum (FWHM), each of which conveys different physical information. The Raman shift corresponds to vibrational energies and is primarily used for chemical identification and structural information. The peak intensity or peak area is related to the concentration of scatterers and the Raman cross section, and can also reflect enhancement effects due to resonance [35]. The FWHM provides information about lifetime broadening, disorder, crystallinity, and interactions (e.g., phonon scattering or temperature effects). To extract these parameters accurately, an appropriate fitting model (such as Lorentzian, Gaussian, or Voigt profile) must be chosen depending on the underlying physical broadening mechanisms. Lorentzian profiles are typically associated with homogeneous broadening (lifetime effects), while Gaussian profiles describe

inhomogeneous broadening (e.g., disorder). If the goal is to determine only the Raman shift (peak position), the choice of fitting function generally does not strongly affect the result, provided the peak is symmetric and well-resolved; however, for precise analysis of FWHM or peak area, the choice of model becomes important and must reflect the physical origin of the line shape.

Results and discussion 4

In the Raman spectroscopy measurements presented here, several experimental challenges must be carefully considered to ensure reliable interpretation of the results. Particular attention must be given to the sample integrity, as improper laser conditions such as excessive power or unsuitable wavelength can induce thermal damage or alter the material's properties.

Optimizing these parameters is therefore essential to obtain high quality spectra while preserving the sample integer. Furthermore, the assignment of Raman peaks to specific vibrational modes can be nontrivial, requiring thorough comparison with literature and a solid understanding of the system under study. In many cases, overlapping features require peak deconvolution to accurately resolve individual contributions. Additionally, the interpretation of the data must take into account that computational methods, such as density functional theory (DFT), often overestimate vibrational frequencies due to inherent approximations (e.g., the harmonic approximation), which can complicate direct comparison with experimental spectra. Together, these factors highlight the importance of careful experimental design and critical analysis in the discussion of Raman results.

4.1 Peak assignment

Peak assignment in Raman spectroscopy is essential because it enables the direct correlation between vibrational features and specific molecular motions, allowing structural changes, temperature phenomena, doping effects, and variations in the electronic state of conjugated polymers to be accurately identified and interpreted.

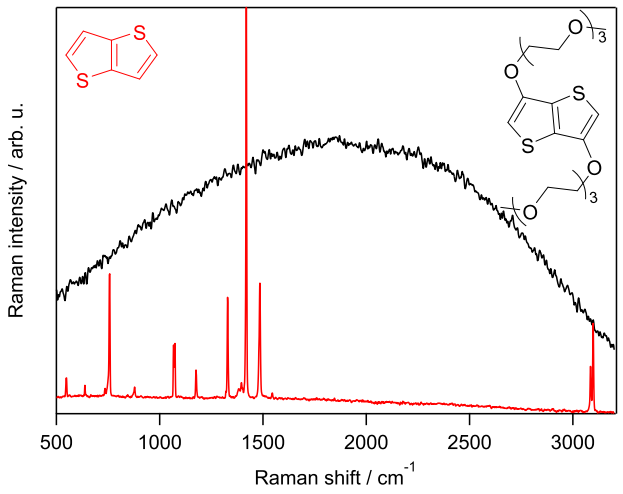

Figure 4.1: Illuminated Raman spectrum of g_3TT (black trace), dominated by fluorescence background and consequently poorly resolved, compared with a well-resolved TT spectrum (red trace).

A detailed peak assignment is provided in Paper I. As observed in this study, not all compounds could be directly investigated using Raman spectroscopy. In particular, g_3TT (see Figure 4.1 for chemical structure) exhibited strong fluorescence, which obscured the Raman signal and hindered spectral analysis (Figure 4.1). To overcome this limitation, an isomeric compound without side chains was examined instead, enabling the acquisition of clearer and more interpretable Raman spectra.

In addition, the evolution of the Raman spectra across the polymeric series was investigated as the number of thienothiophene rings increased (Figure 4.2). The experimental data show good agreement and reveal a progressive red shift with increasing chain length. Such observations are crucial for peak assignment, particularly in our case where thienothiophene is used as one of the fundamental building blocks.

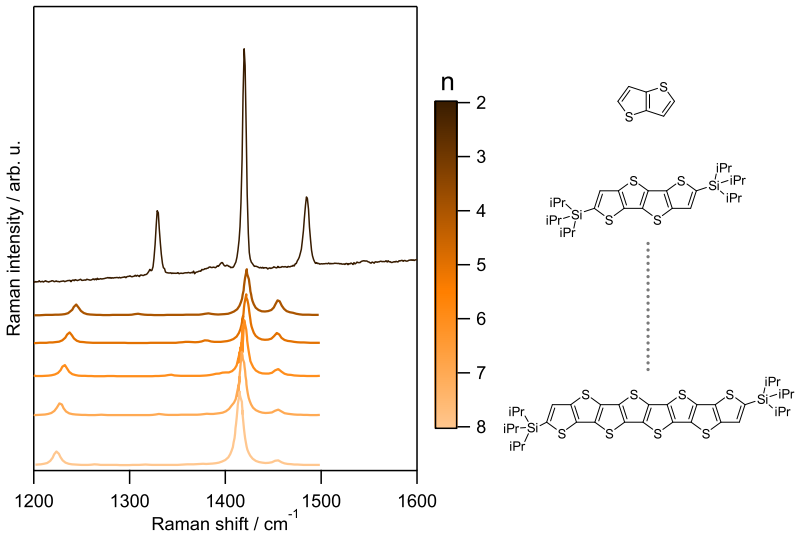

Figure 4.2: Raman spectra of thienothiophene-based oligomers as a function of chain length (n). The spectrum of thienothiophene (T2) was measured experimentally, while spectra for oligothienoacenes (T_n, $n = 4 - 8$ (color coded as index n)) were obtained from literature-reported computational data [37].

4.1.1 Computational and experimental approach

For a detailed peak assignment, two complementary approaches can be employed: density functional theory (DFT) calculations and experimental analysis.[1] While DFT provides valuable insight into the fundamental vibrational modes, experimental Raman spectroscopy offers direct access to the actual response of the system. In this work, the assignment was primarily guided by experimental data, ensuring that the observed spectral features reflect the real structural and environmental conditions of the samples.

1: DFT calculations assume that the potential energy surface is purely harmonic while real molecular vibrations are anharmonic [38].

4.2 Temperature-dependent Raman spectroscopy

Temperature-dependent Raman spectroscopy is a powerful tool for probing structural and dynamical changes in materials, as it provides direct access to the evolution of vibrational modes as a function of temperature. Variations in peak position, linewidth, and intensity reflect changes in intermolecular interactions, anharmonic effects, and structural rearrangements within the system.

One of the key advantages of this technique is its sensitivity to relaxation processes. As the temperature approaches characteristic transitions such as the glass transition temperature (T_g), the vibrational spectrum exhibits measurable changes such as peak intensity fluctuation, peak broadening and shifts, which are associated with increased molecular mobility and the onset of structural relaxation processes.

In Paper I, temperature-dependent Raman measurements were used to monitor the evolution of specific vibrational modes across a defined temperature range. By tracking changes in peak position and peak intensity, insights into relaxation dynamics were obtained. In particular, the analysis of the backbone and the side-chain modes and their temperature dependence provides information on collective motions and local rearrangements, which are directly linked to the relaxation processes occurring in the material.

Thus, temperature-dependent Raman spectroscopy enables the correlation of microscopic vibrational behavior with macroscopic relaxation phenomena, offering a valuable approach for understanding the dynamic properties of conjugated polymers.

In temperature-dependent Raman experiments, silicon (Si) substrates are particularly advantageous due to their high thermal conductivity[2], which ensures efficient heat dissipation and uniform temperature distribution. Additionally, the well-defined and nearly linear temperature dependence of the Si Raman peak position[3] at 520.6 cm^{-1} due to thermal expansion (Figure 4.3) can be used as an internal thermometer to accurately monitor the local sample temperature during measurements.

2: For Si, $k_{Si} \approx 100\ W\,m^{-1}\,K^{-1}$, while for conjugated polymers $k \approx 0.1$–$0.5\ W\,m^{-1}\,K^{-1}$ [39].

3: An additional observation is the peak broadening, which is associated with increased lattice anharmonicity and a shortening of the phonon lifetime as the temperature increases [40].

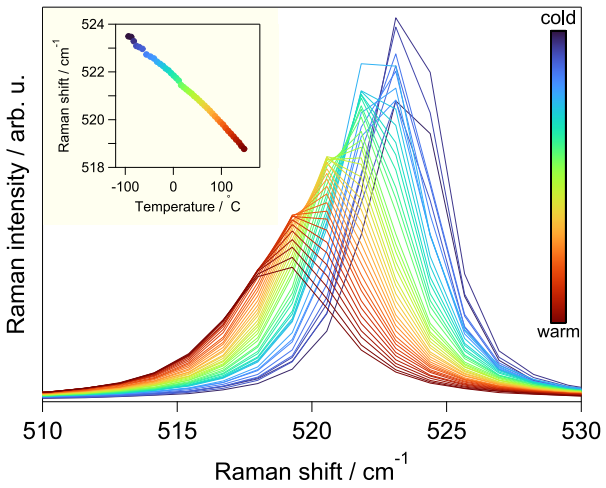

Figure 4.3: Temperature-dependent Raman spectra of silicon, recorded from −100 to 150 °C, showing a systematic peak shift. Inset: peak position as a function of temperature.

4.3 Doping and Raman spectroscopy

In this section, the aim is to highlight how the doping state of a conjugated polymer can be experimentally identified. During the doping process, the formation of poralons leads to a distortion of the molecular structure. This structural modification is reflected in Raman spectroscopy, typically observed as shifts in Raman–active vibrational modes or changes in their relative intensities, due to the accompanying reduction of the electronic bandgap.

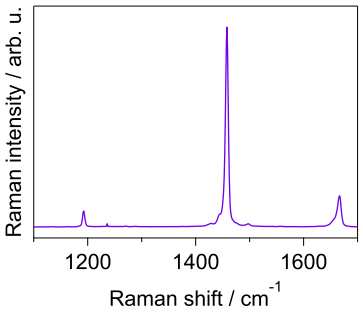

Figure 4.4: Raman spectrum of the dopant F4TCNQ.

4: F4TCNQ induces doping via a charge-transfer mechanism, often giving rise to characteristic vibrational modes of the dopant in the Raman spectrum. In contrast, LiTFSI doping proceeds via an anion-exchange mechanism, where no strongly Raman-active charge-transfer complex is formed.

In the case of chemical doping certain dopant molecules, such as F4TCNQ, exhibit characteristic vibrational signatures that can be directly detected in the Raman spectra (see Figure 4.4 for pure dopant and Figure 4.5 for doped polymer). In contrast, for dopants such as LiTFSI, no distinct additional Raman peaks are typically observed, indicating a different interaction mechanism[4] or extremely weaker Raman activity of the dopant species relatively to the host polymer.

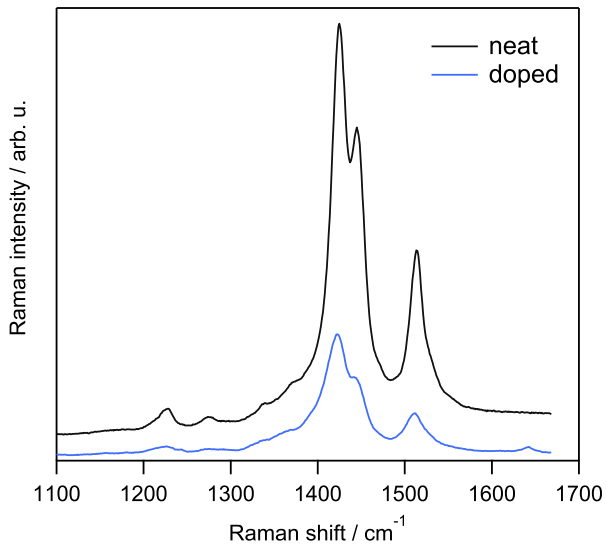

Figure 4.5: Raman spectrum of the neat p(g_3TT-T2) (black trace) and of p(g_3TT-T2) doped with F4TCNQ (blue trace).

In this field, it is common to analyze the intensity ratios between

Raman modes associated with the polymer backbone (–C=C–), due to their high intensity and their origin in π-conjugated orbitals, as these provide a reliable indicator of the degree of π-orbital delocalization induced by doping (Paper II).

4.4 Spatial mapping

Raman mapping is performed to spatially resolve variations in the doping level across the sample (Figure 4.6) and to capture local heterogeneities that cannot be observed in single point measurements. In Paper II, this approach reveals the presence of lateral doping gradients, indicating that the doping process is preferentially enhanced over the gold channels upon introduction of a persulfonic solution.

Raman mapping can be performed over the x-y plane, as demonstrated in Paper II, to resolve lateral variations. In addition, depth-dependent measurements can also be carried out to investigate how the doping level and structural properties evolve through the thickness of the film.[5]

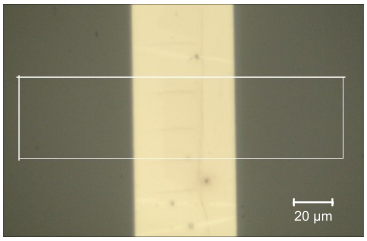

Figure 4.6: Picture under the microscope of the polymer PBTTT deposited onto the gold electrode as an example of the mapped region.

5: An important parameter determining the spatial resolution is the instrumental setup. See Appendix A, *Optical parameters in Raman microscopy*, for an estimation of the achievable spatial resolutions (laterally and in-depth).

Conclusions and future work 5

5.1 Summary of key findings

In Paper I, Raman spectroscopy was employed to investigate the vibrational modes of the conjugated polymer p(g_3TT-T2). A detailed experimental assignment of Raman-active modes was carried out, enabling the identification of specific vibrational signatures associated with both the polymer backbone and the triethylene glycol side chains. Temperature-dependent Raman measurements were further used to probe the glass transition, providing insight into the structural dynamics of the material. This approach establishes a robust framework for interpreting Raman spectra in conjugated polymers with polar glycol ether side chains and for linking spectroscopic features to relaxation phenomena and the glass transition.

Paper II demonstrates a doping mechanism that is inherently spatially non-uniform, originating at the gold interface and propagating laterally through the film. Raman mapping provides a powerful means to resolve these variations, enabling direct visualization of the resulting doping gradients across the sample. By monitoring spatial changes in intensity ratios associated with the polymer backbone, the evolution of the local doping level can be tracked with micrometer resolution. This approach reveals that the doping process is preferentially enhanced near the gold electrodes, highlighting the critical role of interfaces in governing the distribution of charge carriers. Such spatially resolved spectroscopic analysis is essential for understanding and controlling doping in real devices, where local heterogeneities strongly influence electronic performance.

5.2 Open questions

Despite the insights gained, several open questions remain regarding the interplay between doping and structural dynamics. In particular, it is not yet fully understood how the T_g evolves upon doping. The introduction of charge carriers and counterions may alter chain mobility, free volume, and intermolecular interactions, potentially leading to either plasticization or stiffening of the polymer matrix.

Furthermore, temperature-dependent Raman spectroscopy of doped systems raises important questions about what information can be extracted from the dopant-related vibrational modes. In the case of F4TCNQ, shifts in characteristic peaks with temperature may provide insight into the stability of the charge-transfer

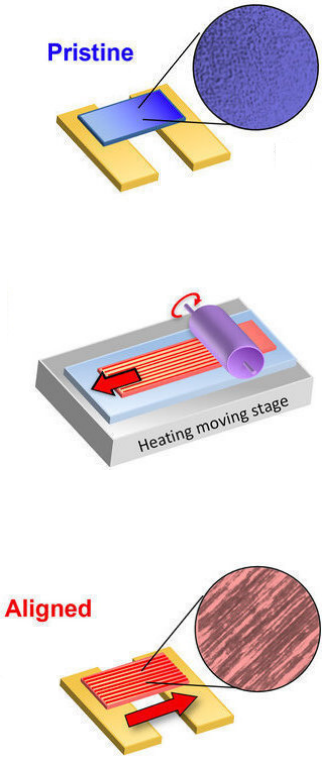

Figure 5.1: Schematic illustration of (top, blue) a pristine, non-aligned film and (bottom, red) an aligned film after the alignment process. Adapted from Ref. [41].

complex, changes in the degree of charge transfer, and the coupling between the dopant and the polymer backbone. Understanding these temperature-dependent spectral signatures could offer a direct probe of how electronic interactions and structural dynamics evolve across the glass transition in doped conjugated polymers.

5.3 Ideas for future work

To further extend the work conducted so far, a promising direction would be to investigate aligned polymer films using polarized Raman spectroscopy. This will provide insight into the anisotropy of vibrational modes and their relation to molecular orientation and chain ordering. This approach could help quantify structural alignment and correlate spectroscopic signatures with charge transport properties. Another case could be investigating conjugated polymers under electrochemical doping conditions using in-situ Raman spectroscopy to enable real-time monitoring of structural and electronic changes. Such measurements could reveal the evolution of polaronic and bipolaronic states, track doping-induced shifts in vibrational modes, and provide a deeper understanding of the dynamics and stability of doped states in functional devices.

Bibliography

(1) S. G. Thulin, US3180557A, S. Aktiebolaget Celloplast, Norrköping, Filed July 10, 1962. US Patent, 1965 (cit. on p. 1).

(2) M. F. Ashby, in *Materials and the Environment (Second Edition)*, Butterworth-Heinemann, Boston, Second Edition, 2013, pp. 459–595 (cit. on p. 1).

(3) S. Ash, R. Sharma and M. Rabnawaz, *Industrial & Engineering Chemistry Research*, 2024, **63**, 22287–22297 (cit. on p. 1).

(4) T. M. Krygowski and B. T. Stpień, *Chemical Reviews*, 2005, **105**, PMID: 16218559, 3482–3512 (cit. on p. 1).

(5) J. W. Moore, *Journal of Chemical Education*, 2001, **78**, 8 (cit. on p. 1).

(6) G. Prunet, F. Pawula, G. Fleury, E. Cloutet, A. Robinson, G. Hadziioannou and A. Pakdel, *Materials Today Physics*, 2021, **18**, 100402 (cit. on p. 1).

(7) S. H. K. Paleti, S. Haraguchi, Z. Cao, M. Craighero, J. Kimpel, Z. Zeng, P. Sowinski, D. Zhu, J. Pons i Tarrés, Y. Kim, Q. Li, J. Huang, A. Kalaboukhov, B. Mihiretie, S. Fabiano, X. Gu and C. Müller, *Macromolecules*, 2025, **58**, 3578–3588 (cit. on p. 1).

(8) X. Wu, W. Fu and H. Chen, *ACS Applied Polymer Materials*, 2022, **4**, 4609–4623 (cit. on p. 2).

(9) A. Aldulaimi, S. M. Saeed, S. V. Menon, R. Y. Saber, S. Ray, K. Jayabalan, A. Sinha, R. Sharma, W. M. Taher and M. Alwan, *RSC Adv.*, 2025, **15**, 45245–45267 (cit. on p. 2).

(10) Heliatek GmbH, *Heliatek – Organic Solar Films*, Accessed 19 May 2026, 2026 (cit. on p. 2).

(11) G. Dufil, I. Bernacka-Wojcik, A. Armada-Moreira and E. Stavrinidou, *Chemical Reviews*, 2022, **122**, PMID: 34928592, 4847–4883 (cit. on p. 2).

(12) J.-L. Brédas, D. Beljonne, V. Coropceanu and J. Cornil, *Chemical Reviews*, 2004, **104**, PMID: 15535639, 4971–5004 (cit. on p. 2).

(13) A. Facchetti, *Chemistry of Materials*, 2011, **23**, 733–758 (cit. on p. 3).

(14) S. S. Zade, N. Zamoshchik and M. Bendikov, *Accounts of Chemical Research*, 2011, **44**, PMID: 20942477, 14–24 (cit. on p. 3).

(15) J. L. Bredas and G. B. Street, *Accounts of Chemical Research*, 1985, **18**, 309–315 (cit. on p. 3).

(16) K. Müllen and U. Scherf, *Macromolecular Chemistry and Physics*, 2023, **224**, 2200337 (cit. on p. 3).

(17) R. Kroon, D. A. Mengistie, D. Kiefer, J. Hynynen, J. D. Ryan, L. Yu and C. Müller, *Chem. Soc. Rev.*, 2016, **45**, 6147–6164 (cit. on p. 4).

(18) C. K. Chiang, C. R. Fincher, Y. W. Park, A. J. Heeger, H. Shirakawa, E. J. Louis, S. C. Gau and A. G. MacDiarmid, *Physical Review Letters*, 1977, **39**, 1098–1101 (cit. on p. 4).

(19) D. Scheunemann, C. Melzer et al., *Chemical Physics Reviews*, 2022, **3**, 021304 (cit. on p. 4).

(20) K. Namsheer and C. S. Rout, *RSC Advances*, 2021, **11**, 5659–5697 (cit. on p. 4).

(21) In *Collected Papers of L.D. Landau*, ed. D. TER HAAR, Pergamon, 1965, pp. 67–68 (cit. on p. 4).

(22) M. Craighero, M. Jha, E. V. Flores-Vela, J. Kimpel, A. Schaefer, J. Guo, J. Asatryan, A. P. Veiga, S. Haraguchi, P.-A. Carlsson, J. Martín, M. Campoy-Quiles and C. Müller, *Advanced Functional Materials*, 2026, **36**, e25493 (cit. on p. 4).

(23) B. Zayat, P. Das, B. C. Thompson and S. R. Narayan, *The Journal of Physical Chemistry C*, 2021, **125**, 7533–7541 (cit. on p. 4).

(24) S. T. Keene, J. E. M. Laulainen, R. Pandya, M. Moser, C. Schnedermann, P. A. Midgley, I. McCulloch, A. Rao and G. G. Malliaras, *Nature Materials*, 2023, **22**, 1121–1127 (cit. on p. 5).

(25) D. T. Tran, A. Gumyusenge, X. Luo, M. Roders, Z. Yi, A. L. Ayzner and J. Mei, *ACS Applied Polymer Materials*, 2020, **2**, 91–97 (cit. on p. 6).

(26) L. Yu, E. Davidson, A. Sharma, M. R. Andersson, R. Segalman and C. Müller, *Chemistry of Materials*, 2017, **29**, PMID: 28713199, 5654–5662 (cit. on p. 6).

(27) Z. Zhang, Q. Chen, J. Wang, C. Xiao, Z. Tang, C. R. McNeill and W. Li, *Giant*, 2024, **19**, 100322 (cit. on p. 6).

(28) C. Panayiotou, *Polymers*, 2024, **16**, 298 (cit. on p. 7).

(29) M. Giordano, M. Russo, P. Capoluongo, A. Cusano and L. Nicolais, *Journal of Non-Crystalline Solids*, 2005, **351**, 515–522 (cit. on p. 7).

(30) S. Luo, T. Wang, M. U. Ocheje, S. Zhang, J. Xu, Z. Qian, X. Gu, G. Xue, S. Rondeau-Gagné, J. Jiang, W. Hu, E. Zhuravlev and D. Zhou, *Macromolecules*, 2020, **53**, 4480–4489 (cit. on p. 7).

(31) C. Angell, *Journal of Non-Crystalline Solids*, 1985, **73**, 1–17 (cit. on pp. 7, 28).

(32) M. Arnoult, E. Dargent and J. Mano, *Polymer*, 2007, **48**, 1012–1019 (cit. on p. 7).

(33) E. Laredo, N. Suarez, A. Bello, B. Rojas de Gáscue, M. Gomez and J. Fatou, *Polymer*, 1999, **40**, 6405–6416 (cit. on p. 8).

(34) A. Jablonski, *Nature*, 1933, **131**, 839–840 (cit. on p. 10).

(35) P. J. Larkin, in *Infrared and Raman Spectroscopy*, Elsevier, Second Edition, 2018, pp. 85–134 (cit. on pp. 10, 12, 27).

(36) Renishaw plc, *What is Raman scattering*, https://www.renishaw.com/pt/what-is-raman-scattering--25805, Accessed 19 May 2026, 2024 (cit. on p. 11).

(37) R. Malavé Osuna, V. Hernández, J. T. López Navarrete, J. Aragó, P. M. Viruela, E. Ortí, Y. Suzuki, S. Yamaguchi, J. T. Henssler and A. J. Matzger, *ChemPhysChem*, 2009, **10**, 3069–3076 (cit. on p. 16).

(38) L. Hou, Y. Liu, X. Song, K. Wang, Y. Zhang, B. Zhang and S. Wang, *Langmuir*, 2024, **40**, PMID: 39615050, 25997–26006 (cit. on p. 16).

(39) X. Rodríguez-Martínez, F. Saiz, B. Dörling, S. Marina, J. Guo, K. Xu, H. Chen, J. Martin, I. McCulloch, R. Rurali, J. S. Reparaz and M. Campoy-Quiles, *Advanced Energy Materials*, 2024, **14**, 2401705 (cit. on p. 17).

(40) C. B. Saltonstall, J. Serrano, P. M. Norris, P. E. Hopkins and T. E. Beechem, *Review of Scientific Instruments*, 2013, **84**, 064903 (cit. on p. 17).

(41) O. Bardagot, P. Durand, S. Guchait, H.-Y. Wu, I. Heinzen, W. Errafi, V. Bouylout, A. Pistillo, C.-Y. Yang, G. Rebetez, P. Cavassin, B. Jismy, J. Réhault, S. Fabiano, M. Brinkmann, N. Leclerc and N. Banerji, *Advanced Materials*, 2025, **37**, 2420323 (cit. on p. 22).

(42) Edinburgh Instruments, *Diffraction Grating Selection for Raman Spectroscopy*, https://edin.b-cdn.net/wp-content/uploads/2021/10/TN_R02_Grating_Selection_Raman_Spectroscopy-1.pdf, Application Note TN-R02, Accessed 19 May 2026, 2021 (cit. on p. 27).

(43) M. J. Baker, C. S. Hughes and K. A. Hollywood, in *Biophotonics: Vibrational Spectroscopic Diagnostics*, Morgan Claypool Publishers, 2016, 3-1 to 3–13 (cit. on p. 28).

(44) M. Mours and H. Winter, in *Experimental Methods in Polymer Science*, ed. T. Tanaka, Academic Press, Boston, 2000, pp. 495–546 (cit. on p. 28).

Appendix

Appendix A

1 Infrared spectroscopy

A vibrational mode is infrared active if it induces a change in the molecular dipole moment during vibration [35]:

$$\left(\frac{\partial \mu}{\partial Q}\right) \neq 0$$

where μ is the molecular dipole moment and Q is the normal vibrational coordinate.

As a result, infrared spectroscopy is particularly sensitive to:

- Polar bonds and functional groups
- Asymmetric vibrational modes
- Local chemical environments

Table A.1: Comparison between Raman and infrared spectroscopy

Aspect	**Raman Spectroscopy**	**Infrared (IR) Spectroscopy**
Physical process	Inelastic light scattering	Absorption of IR radiation
Selection rule	Change in polarizability	Change in dipole moment
Activity condition	$(\partial\alpha/\partial Q) \neq 0$	$\left(\partial\mu/\partial Q\right) \neq 0$
Strong for	Symmetric vibrations	Asymmetric vibrations
Sensitivity	Non-polar, conjugated bonds	Polar bonds, functional groups
Typical source	Visible / NIR laser	IR source
Water sensitivity	Low	High
Complementarity	Often weak in IR	Often weak in Raman

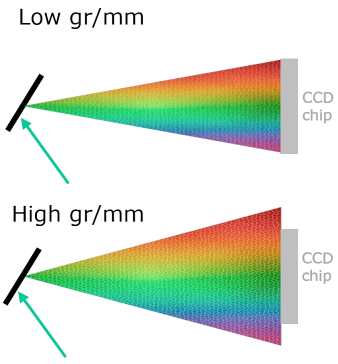

Figure A.1: Dispersion of light by gratings with low (top) and high (bottom) groove densities; from Ref. [42].

2 Optical parameters in Raman microscopy

The objective lens in a Raman microscope plays a central role in both focusing the excitation laser onto the sample and collecting the weak Raman-scattered light. Its properties therefore strongly influence spatial resolution and signal collection efficiency [43].

The performance of a Raman system is primarily governed by the Numerical Aperture (NA), defined as:

$$NA = n \sin(\theta) \tag{1}$$

where n is the refractive index of the medium between the objective lens and the sample (e.g., $n \approx 1$ for air, ~ 1.33 for water, and higher for immersion oils) and θ is the half-angle of the maximum cone of light that can enter or exit the objective lens.

The spatial resolution, both laterally (Δxy) and axially (Δz), is thus determined by the laser wavelength (λ) and the NA:

$$\Delta xy = \frac{0.61\lambda}{NA} \tag{2}$$

$$\Delta z = \frac{2n\lambda}{NA^2} \tag{3}$$

Larger NA values lead to higher spatial resolution (smaller focal spots) in both lateral and axial directions.

Furthermore, the collection efficiency of the Raman signal (I) is directly proportional, apart from the λ^{-4} dependence of Raman scattering, to the square of the NA:

$$I \propto NA^2 \tag{4}$$

Thus, objectives with higher NA not only improve spatial resolution but also significantly enhance the collected Raman signal.

3 Connection between fragility (Angell) and Williams–Landel–Ferry (WLF)

The WLF equation is widely used to describe the temperature dependence of relaxation dynamics near the glass transition and provides a convenient framework to quantitatively relate time–temperature superposition to the concept of fragility.

WLF equation (shift factor) [44]:

$$\log(a_T) = -\frac{C_1(T - T_g)}{C_2 + (T - T_g)} \tag{5}$$

Time–temperature superposition relation [44]:

$$\log(\tau(T)) = \log(\tau(T_g)) + \log(a_T) \tag{6}$$

Definition of fragility [31]:

$$m = \left. \frac{d \log_{10}(\text{relaxation})}{d(T_g/T)} \right|_{T=T_g} \tag{7}$$

Change of variable:

$$x = \frac{T_g}{T} \tag{8}$$

$$\Rightarrow \left.\frac{d}{dx}\right|_{x=1} = -T_g \left.\frac{d}{dT}\right|_{T=T_g} \tag{9}$$

Relation to shift factor:

$$m = -T_g \left.\frac{d\log(a_T)}{dT}\right|_{T=T_g} \tag{10}$$

Differentiate WLF form:

$$\log(a_T) = -\frac{C_1(T - T_g)}{C_2 + (T - T_g)} \tag{11}$$

$$Let\ y = T - T_g \tag{12}$$

$$\log(a_T) = -\frac{C_1 y}{C_2 + y} \tag{13}$$

$$\frac{d\log(a_T)}{dy} = -C_1 \frac{(C_2 + y) - y}{(C_2 + y)^2} = -C_1 \frac{C_2}{(C_2 + y)^2} \tag{14}$$

Evaluate at T = T_g (i.e., y = 0)

$$\left.\frac{d\log(a_T)}{dT}\right|_{T=T_g} = -\frac{C_1}{C_2} \tag{15}$$

Final fragility expression:

$$m = -T_g \left(-\frac{C_1}{C_2}\right) = \frac{C_1 T_g}{C_2} \tag{16}$$

As seen from the final expression, the fragility m emerges as a dimensionless parameter determined by the ratio of the WLF constants, linking macroscopic relaxation behavior directly to empirical thermorheological parameters.

Appended Papers